FRONTIERS OF PHYSICS

RESEARCH ARTICLE
Volume 18 / Issue 6 / 63301 / 2023

Reconfigurable memristor based on $SrTiO_3$ thin-film for neuromorphic computing

Xiaobing Yan[1,*,†], Xu Han[1,*], Ziliang Fang[1], Zhen Zhao[1], Zixuan Zhang[1], Jiameng Sun[1], Yiduo Shao[1], Yinxing Zhang[1], Lulu Wang[1], Shiqing Sun[1], Zhenqiang Guo[1], Xiaotong Jia[1], Yupeng Zhang[1], Zhiyuan Guan[1], Tuo Shi[2,‡]

1 Institute of Life Science and Green Development, Key Laboratory of Brain-Like Neuromorphic Devices and Systems of Hebei Province, College of Electron and Information Engineering, Hebei University, Baoding 071002, China

2 Institute of Microelectronics, Chinese Academy of Sciences, Beijing 100029, China

*These authors contributed equally to the work.

Corresponding authors. E-mail: †yanxiaobing@ime.ac.cn, ‡shituo@zhejianglab.com

Received December 14, 2022; accepted May 2, 2023

© Higher Education Press 2023

ABSTRACT

Neuromorphic computing aims to achieve artificial intelligence by mimicking the mechanisms of biological neurons and synapses that make up the human brain. However, the possibility of using one reconfigurable memristor as both artificial neuron and synapse still requires intensive research in detail. In this work, Ag/$SrTiO_3$(STO)/Pt memristor with low operating voltage is manufactured and reconfigurable as both neuron and synapse for neuromorphic computing chip. By modulating the compliance current, two types of resistance switching, volatile and nonvolatile, can be obtained in amorphous STO thin film. This is attributed to the manipulation of the Ag conductive filament. Furthermore, through regulating electrical pulses and designing bionic circuits, the neuronal functions of leaky integrate and fire, as well as synaptic biomimicry with spike-timing-dependent plasticity and paired-pulse facilitation neural regulation, are successfully realized. This study shows that the reconfigurable devices based on STO thin film are promising for the application of neuromorphic computing systems.

Keywords Ag/STO/Pt reconfigurable memristor, volatile and nonvolatile coexistence, neuron circuit, synaptic biomimicry, neuromorphic computing

1 Introduction

The traditional computer adopts the von Neumann architecture, which suffers from the bottleneck of high power consumption and slow speed [1, 2]. Nowadays, many reports show that brain-like computing can preferably alleviate this problem [3–5]. Amazing breakthroughs in the simulation of brain-like behavior have been achieved [6–9]. The use of memristors in electronic circuits to achieve more efficient development of neuromorphic systems is a subject of intense research. Among them, a memristor has resistance switching (RS) characteristics, and its resistance can be determined by the amount of charge flowing through it. It can store and process information through flexible changes under

*Special Topic: Materials, Mechanisms and Applications of Memristors (Eds.: Xiaobing Yan, Bin Gao & Qi Liu).

external stimuli. RS can be divided into volatile threshold type and nonvolatile bipolar type in terms of brain-like behavior. Reconfigurable devices [10] where the two switching characteristics coexist in one device are critical to build brain-inspired computing hardware [11, 12]. Taking advantage of the fact that the resistance state of the volatile threshold RS is not easy to maintain, it can be used as the threshold switch (TS) for the study of artificial neurons. In the nonvolatile bipolar RS, the artificial synaptic functions have also been successfully simulated due to its continuously adjustable resistance, similar to the change of synaptic weight [13–15]. The combined action of neurons and synapses can establish the cognitive function of brain-like behaviors.

$SrTiO_3$ (STO), as a typical perovskite oxide, has been used in memristors [16–19]. Hou *et al.* [20] studied the different properties of STO-based ultrathin film devices with different top electrodes and implemented multi-level data storage in the device. Hu *et al.* [21] reported the realization of long-term plasticity and synapse emulations in $Ag/SrTiO_3/(La,Sr)MnO_3$ memristors. Xiong *et al.* [22] implemented Bienenstock, Cooper, and Munro learning rules with tunable sliding frequency thresholds in an STO-based resistive second-order memristor. Rahman *et al.* [23] proposed the STO-based resistive switching memory as a decision element for evaluating threshold levels in artificial electronic receptors. However, there have been few reports of using STO thin-film memristor as a configurable device to simulate biological nerves as both artificial synapses and neurons. In particular, compared with polycrystalline films, amorphous materials have a uniform structure without grain boundaries.

In this work, we proposed a reconfigurable device based on STO amorphous film, based on which a device made of Ag/STO/Pt device can be utilized for neuromorphic computing with the low operating voltage. It is found that by adjusting the compliance current (I_{cc}), two stable characteristics of volatile threshold RS and nonvolatile bipolar RS can be obtained. The device with short-term dynamics in TS mode is used to simulate the local gradient potential (LGP) in the designed circuit model. The leaky integrate-and-fire (LIF) function of neurons can be successfully realized. In addition, in the simulation of synaptic plasticity, the functions of long-term potentiation/depression (LTP/LTD), spike-timing-dependent plasticity (STDP), and paired-pulse facilitation (PPF) are successfully demonstrated by the adjustment of synaptic weights. Therefore, the reconfigurable devices based on Ag/STO/Pt show broader development potential for neuromorphic networks.

2 Experimental details

Amorphous STO film was deposited on Pt bottom electrode by pulsed laser deposition (PLD). Use λ Physik Compex Pro 20S Krf excimer lasers (A = 248 nm) with energy 350 mJ and frequency 5 Hz as the laser condition. After controlling the pressure in the chamber to 2×10^{-4} Pa, the temperature of the growth chamber was raised. The STO film was grown at 750℃ and oxygen pressure of 1 Pa for 20 min. Finally, with the help of a 100 μm diameter mask, Ag electrodes were grown on the STO functional layer by DC magnetron sputtering. The device uses Keithley 4200 to test the DC voltage (I–V) curve. Using the Agilent 33250A function/arbitrary waveform generator and the LeCroy WaveRunner 62Xi oscilloscope, measured the pulse characteristics of the device. Observation of surface morphology by atomic force microscope (AFM).

3 Results and discussion

Figure 1(a) shows the memristor structure with $Ag/STO/Pt/Ti/SiO_2/Si$. Si, Pt, STO, and Ag are used as the substrate, bottom electrode, functional layer, and top electrode. The microstructure of device was tested by transmission electron microscopy (TEM) and atomic force microscopy (AFM) in Fig. S1 of the Electronic Supplementary Materials (ESM). It is possible to obtain an STO amorphous layer with a thickness of about 53.0 nm, and the STO Root Mean Square roughness is 908.3 pm. Therefore, STO film is proven to be homogeneous [24]. To test the electrical performance of the device, Ag, and Pt were connected to the positive and negative poles of the device, which form a direct current (DC) scanning test circuit. Interestingly, the device can be reconfigured by changing different I_{cc} to obtain both volatile threshold RS and nonvolatile bipolar RS characteristics. When $I_{cc} = 1 \times 10^{-6}$ A, the current suddenly rises to the I_{cc} at about 1.8 V, which indicates that the device has completed the transition from the high resistance state (HRS) to the low resistance state (LRS), and the current begins to decline at about 1 V. The device exhibits volatile threshold RS characteristics, and the random TS behavior provides favorable conditions for simulating the leaky integration-and-fire function of neurons [25], as shown in Fig. 1(b). By further increasing the compliance current to 1×10^{-3} A, the device exhibits typical nonvolatile bipolar RS characteristics in Fig. 1(c). When the voltage is around 0.3 V, the current is tripped, and then transitioned to I_{cc}. The I–V curve of the device can pass 0 V voltage at LRS and is slowly shut down at around −0.3 V. Thus, the turn on and off under positive and negative voltage would be gained. The Ag conductive filaments lead to two different results, and more details about the mechanism are discussed in Fig. S2 of the ESM. To further verify the stability of the device, Figs. S3(a, d, b, e) show the I–V curves of 100 scanning cycles and logarithmic represen-

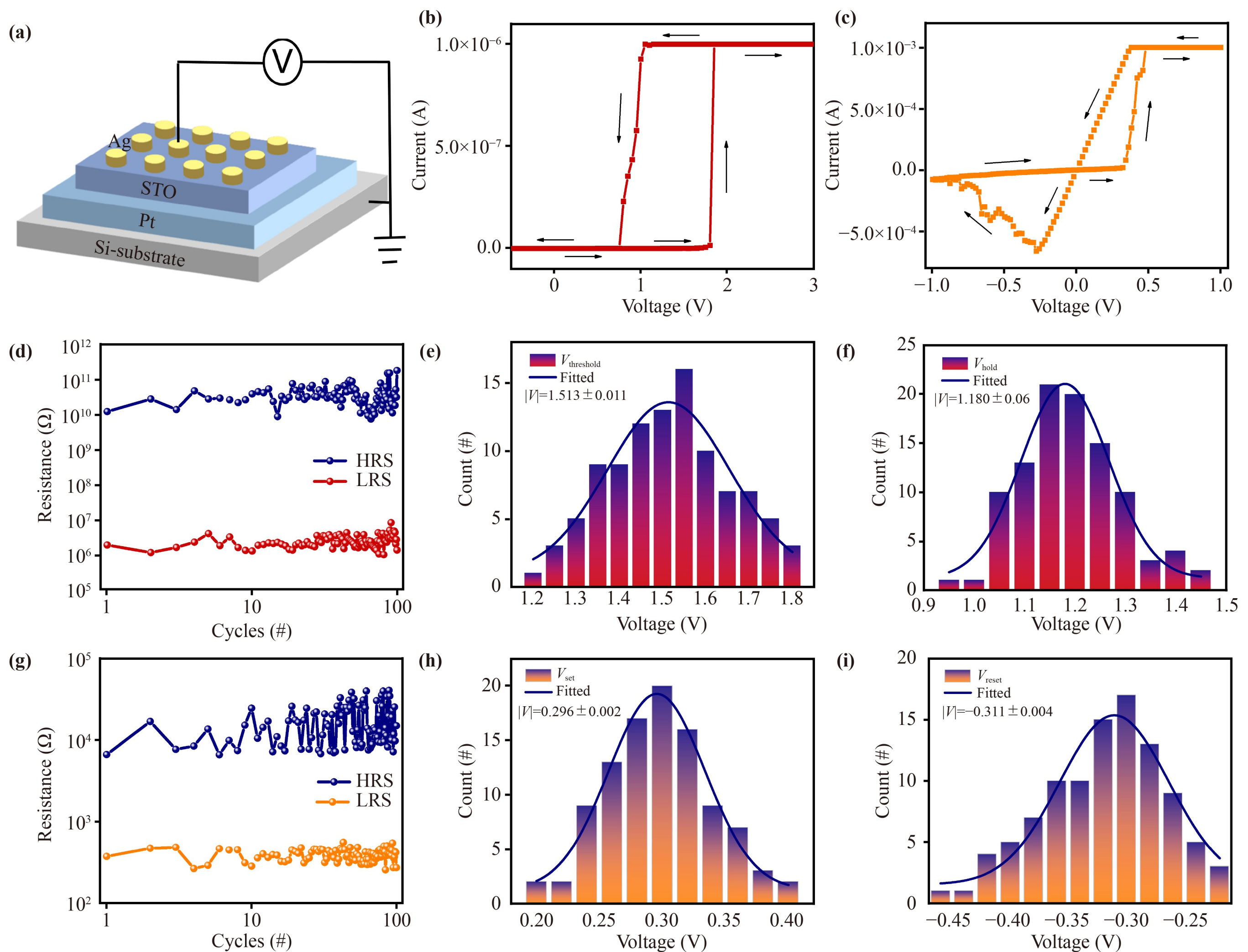

Fig. 1 **(a)** Schematic diagram of Ag/STO/Pt device structure. **(b)** $I_{cc} = 1 \times 10^{-6}$ A, I–V test shows volatile threshold RS characteristics. **(c)** $I_{cc} = 1 \times 10^{-3}$ A, I–V test shows nonvolatile bipolar RS characteristics. **(d, g)** The resistance state distribution of the device over 100 I–V cycles at the volatile threshold RS and nonvolatile bipolar RS. **(e, f)** Threshold and hold voltage distribution statistics. **(h, i)** Set and reset voltage distribution statistics.

tations of $I_{cc} = 1 \times 10^{-6}$ A and $I_{cc} = 1 \times 10^{-3}$ A, respectively. Figures 1(d) and (g) show the distribution of high and low resistance values for volatile threshold and nonvolatile bipolar RS. Gaussian function is used to fit the data of V_{th}, V_{hold}, V_{set}, and V_{reset}, and the cumulative probability is calculated [Figs. S3(c, f)]. These voltages fluctuate in a small range, which conforms to the Gaussian distribution law. The peak values of V_{th} and V_{hold} are about 1.55 V and 1.15 V in Figs. 1(e) and (f). Moreover, it can be concluded that the peak values of V_{set} and V_{reset} are about 0.3 V and −0.3 V, as shown in Figs. 1(h) and (i). In addition, the switching voltage is smaller than other reports [26–28]. Thus, it provides a device with satisfactory performance for the subsequent specific testing and circuit design research.

In order to verify the effect of different bias voltages on volatile threshold characteristics, the relaxation and retention characteristics tests were performed on Ag/STO/Pt device [29]. After the stimulation pulses are applied to the device, reading pulses at different intervals are applied to observe the "relaxed" characteristic of the stimulus. In Fig. 2(a), the device responds to stimulus pulses ($V = 2$ V), and the different voltage responses in the device are observed under the reading pulses ($V = 0.6$ V). As the interval time increases, the device gradually shuts down and completely relaxes to HRS at the interval of 600 μs. When the stimulus pulses are applied to the device, with the increase of the interval time, the responses of the device gradually decrease under the reading pulse and basically relaxes to the HRS device at the interval of 600 μs, as shown in Fig. 2(b). This indicates that the conductive filament dissipates spontaneously, showing significant volatile threshold characteristics. However, when the amplitudes of the applied stimulus

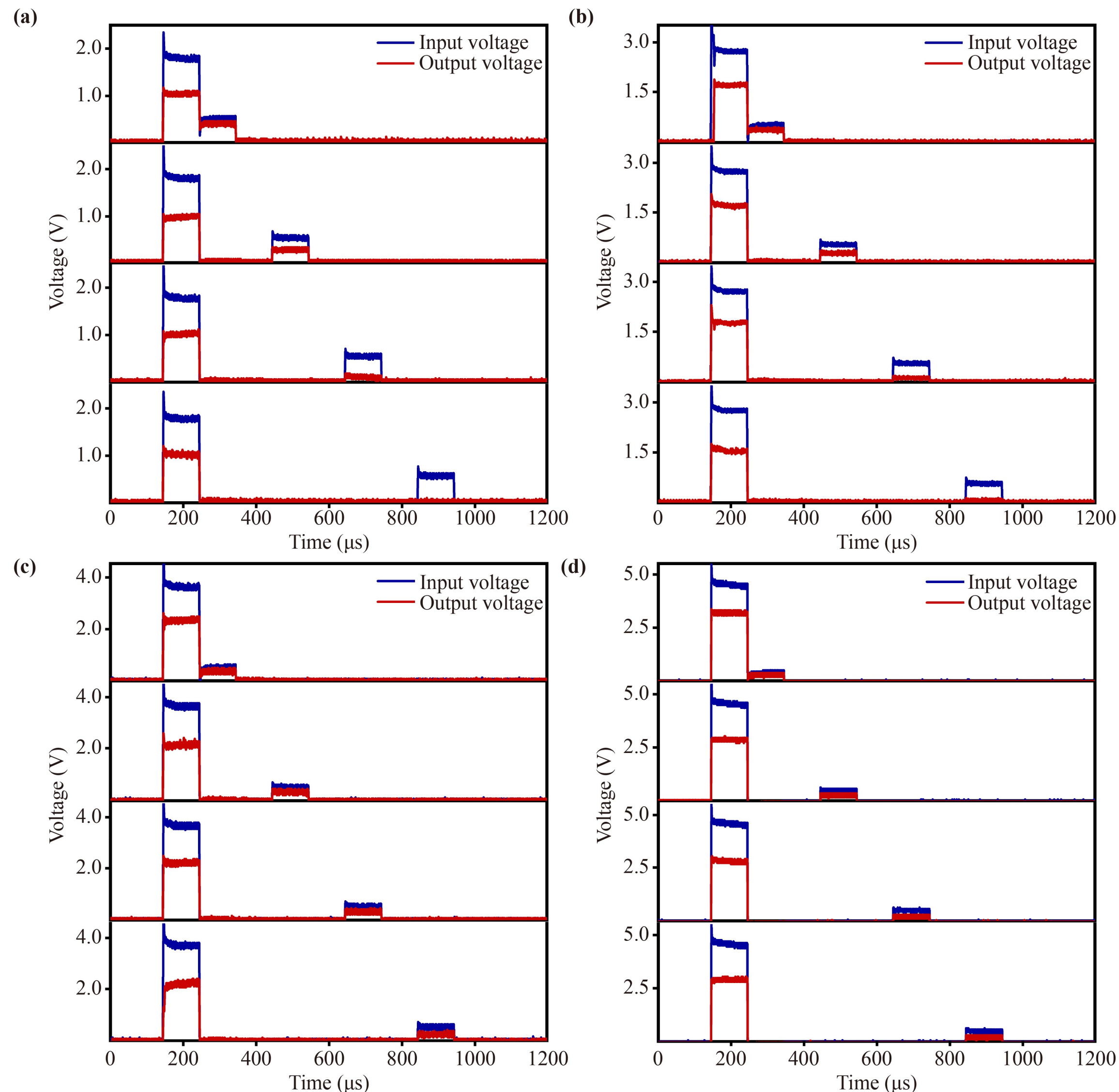

Fig. 2 The transition from volatile to nonvolatile at Ag/STO/Pt device. **(a, b)** Relaxation characteristic of using 2 V and 3 V stimulation pulses. **(c, d)** Retention characteristic of using 4 V and 5 V stimulation pulses. In (a)–(d), the reading pulse with the amplitude of 0.6 V is used, and the pulse durations of both the reading pulses and stimulation pulses are 100 μs, The time intervals between the two are 0, 200, 400, and 600 μs.

pulses are increased to 4 V and 5 V [Figs. 2(c) and (d)] and the reading pulses are applied at the same intervals, the responses remain stable and precise. This means that the thicker conductive filament is formed by high voltages and is challenging to break in the functional layer spontaneously [30]. Therefore, this process realizes the transformation from volatile to nonvolatile switching, verifying that the TS characteristic is related to the electric field strength. In the following, the test voltages for the selected TS characteristics are all less than 3 V.

To further investigate the spiking properties of artificial neurons, we implemented the simulation of the essential leaky integration and fire function of neurons [31]. The resistance change of the TS device is an accumulation process, and the conductive filament needs to be formed at a specific pulse intensity. In order to confirm the influence of pulse amplitude, pulse duration (T_{ON}), and pulse interval (T_{OFF}) on delay time (T_{FIRE}), multiple sets of pulses (N_{FIRE}) are applied to the device as shown in Fig. 3, and different spike responses are obtained. In Fig. 3(a), multiple pulses with $V = 2$ V, $T_{\mathrm{OFF}} = 2.5$ μs, and $T_{\mathrm{ON}} = 1$ μs/2 μs/4 μs are applied to the device, and it can be observed that the delay time is inversely proportional to the pulse duration. Figure 3(b) shows that under the same condition, with the decrease of the pulse interval, the fewer the number of FIRE pulses generated by the device and the smaller the integration time required. The above rules are further discussed, the device is applied to ensure that T_{ON} and T_{OFF} are fixed, and the changes between the output response and the

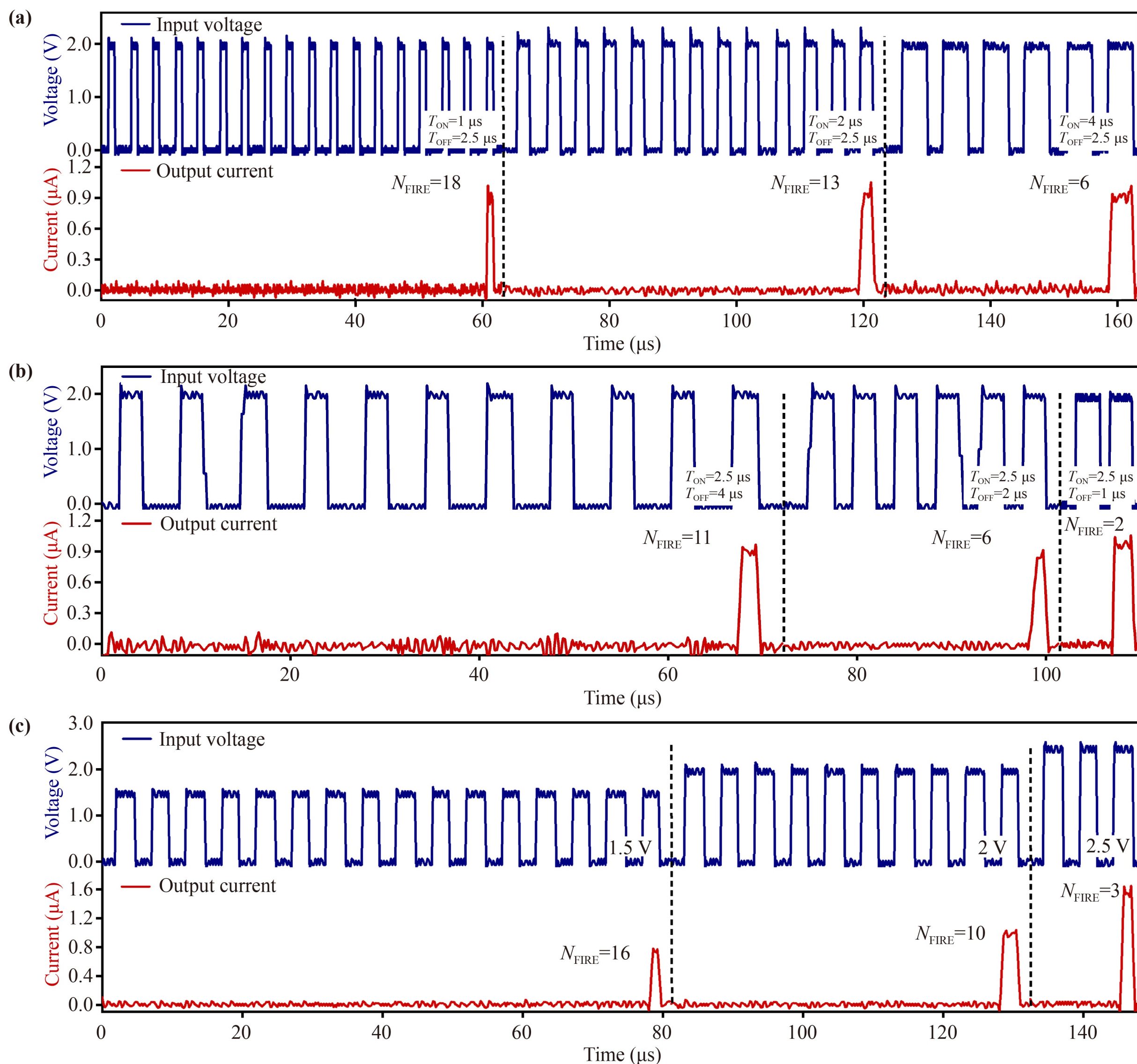

Fig. 3 Change of device T_{FIRE}. **(a)** The interval and amplitude remain unchanged; the N_{FIRE} changes with different pulse durations. **(b)** The pulse duration and amplitude remain unchanged; the N_{FIRE} changes at different intervals. **(c)** The pulse duration and interval remain unchanged; the N_{FIRE} changes with different amplitudes.

input amplitude are observed as shown in Fig. 3(c). It can be seen that the larger the input pulse amplitude, the shorter the time required for the device to produce a spike response. Multiple tests have been carried out for the above different conditions, and the data statistics of the pulses required for FIRE have been performed as shown in Fig. S4 of the ESM. Due to the randomness of the device, the leaky integration and fire function can be realized. Therefore, the experimental results can confirm that with the increase of pulse amplitude and pulse duration, and decrease of pulse interval, the integration process time required by the device decreases, which is the same as the previously reported result [32–34].

Nerve signals are transmitted to neurons through synapses, and the neuron decides whether to pass input information to the next neuron based on the strength of the signals [35]. In biological neurons, differences in LGP result from differences in the concentration of ions inside and outside the cell membrane. Through electrical tests, it can be found that the different intensities of stimulation can regulate the conductance of the Ag/STO/Pt device, which can effectively simulate the LGP changes in neurons [14, 36]. In order to realize the triggering function of biological neurons, we combined the memristor with the peripheral circuit and built the circuit model as shown in Fig. 4(a). The model compares LGP and V_{th} to determine whether neurons can be triggered based on whether the LIF model outputs spikes. The circuit consists of input integration (ADD), Ag/STO/Pt device, comparator (CMP), and TIMER. The input voltages are

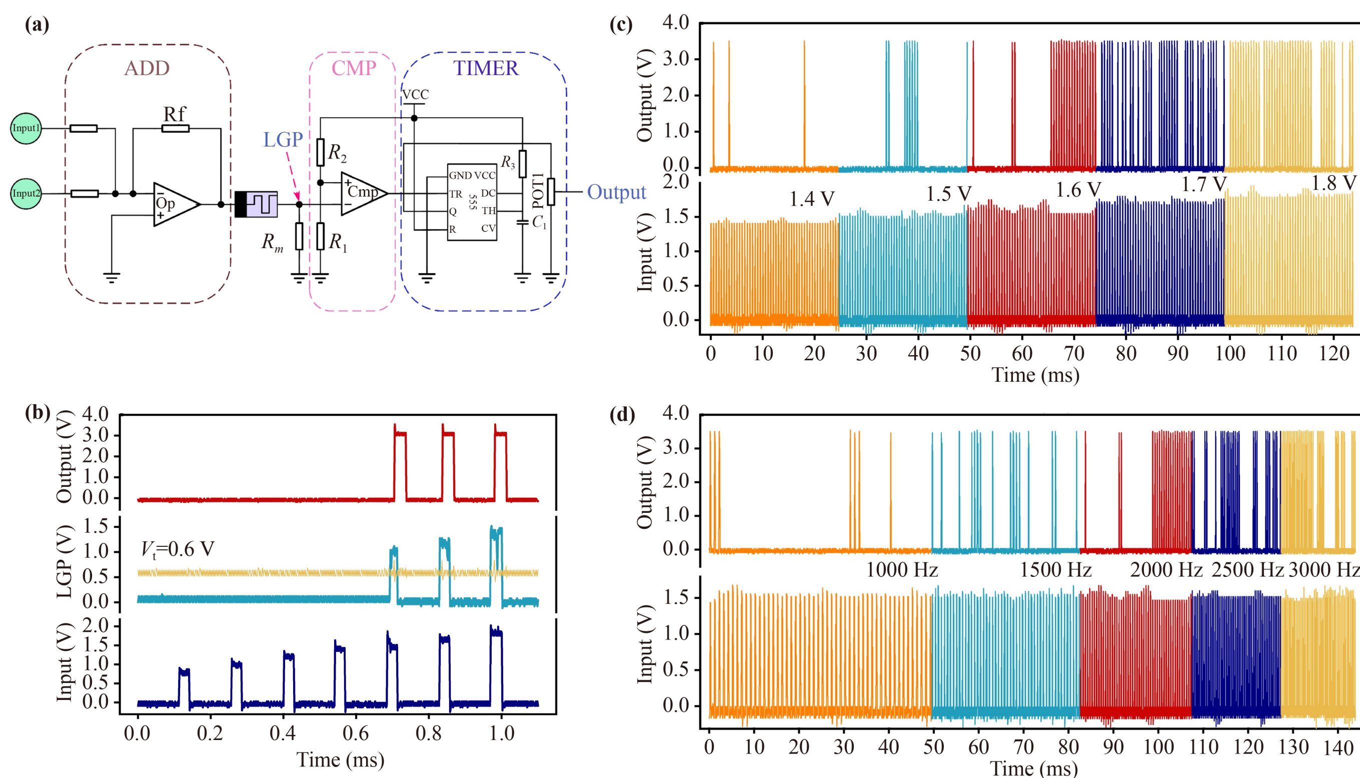

Fig. 4 **(a)** LIF neuron circuit model is realized based on Ag/STO/Pt device. **(b)** Input pulses with different amplitudes, LGP, and circuit output response. **(c)** Response of artificial neuron circuit under input pulses of different voltages. **(d)** Response of artificial neuron circuit under input pulses of different frequencies.

integrated into the STO device, and the LGP is modulated by the different switching states of the device. Different LGPs act on the reverse CMP, then through a monostable trigger, and the whole LIF neuron circuit is finally completed. The monostable generator has two states, stable and transiently stable, and the transition of the two states can be performed under the stimulation of the external pulse. When the input voltage of the generator is less than 1/3 VCC, the timer will flip to 1, enter the transient stable state, and the circuit will trigger the high level with the amplitude of 2/3 VCC. Otherwise, the timer will flip to 0, and the circuit will be in a stable state with the output of low level 0. Setting the supply voltage VCC to 5 V, $V_t = 0.6$ V, and the input voltage with amplitude 0.8–2 V, the output voltage at the LGP and the whole circuit are measured. Figure 4(b) shows the test results, in which the device is triggered at 1.6 V. In the case of LDP $> V_t$, the circuit outputs spiking pulses, which are the firing function of the neuron. When the LGP is below the threshold voltage, the neuron cannot be triggered, indicating that the model leaks in a short period [11]. In biology, there are two modes of spatial and temporal integration of signals passing through synapses [37]. In the circuit, 50 pulses of different amplitudes and 50 pulses of different frequencies are used to simulate the integration of neuron signals in spatial and temporal. Figure 4(c) shows that as the applied voltage is enhanced, the circuit response times are least at 1.4 V and most at 1.8 V. In Fig. 4(d), with the amplitude of 1.6 V and the frequency of 1000–3000 Hz pulses input, it can be obtained that fewer pulses can trigger neurons as the pulse frequency increase. The results show that the test results are consistent with biological neurons [33, 38]. The LIF model designed can complete the simulation of the leaky integrate-and-fire function of biological neurons in spatial and temporal, laying a foundation for studying bionic circuit systems.

When $I_{cc} = 1 \times 10^{-3}$ A, pulse testing with the small pulse duration enabled the simulation of artificial synapses. Switching speed is an essential parameter of bipolar switches [39], so Ag/STO/Pt devices' switching response speeds are tested in Fig. S5 of the ESM. In biological synapses, the intensity of stimulus affects the synaptic weight change. By applying enhancement/suppression pulses with different amplitudes, durations, and intervals to the device, the changes in synaptic weights are simulated with different conductance. Figures 5(a–c) show the dependence of device conductance on positive pulses. When pulses with the duration and interval of 100 ns are applied to the device, the rate of change of the device conductance is proportional to the amplitude of the positive pulses, as shown in Fig. 5(a). Controlling the applied pulses, the amplitude of 2 V, and the interval of 100 ns, it can be observed that the

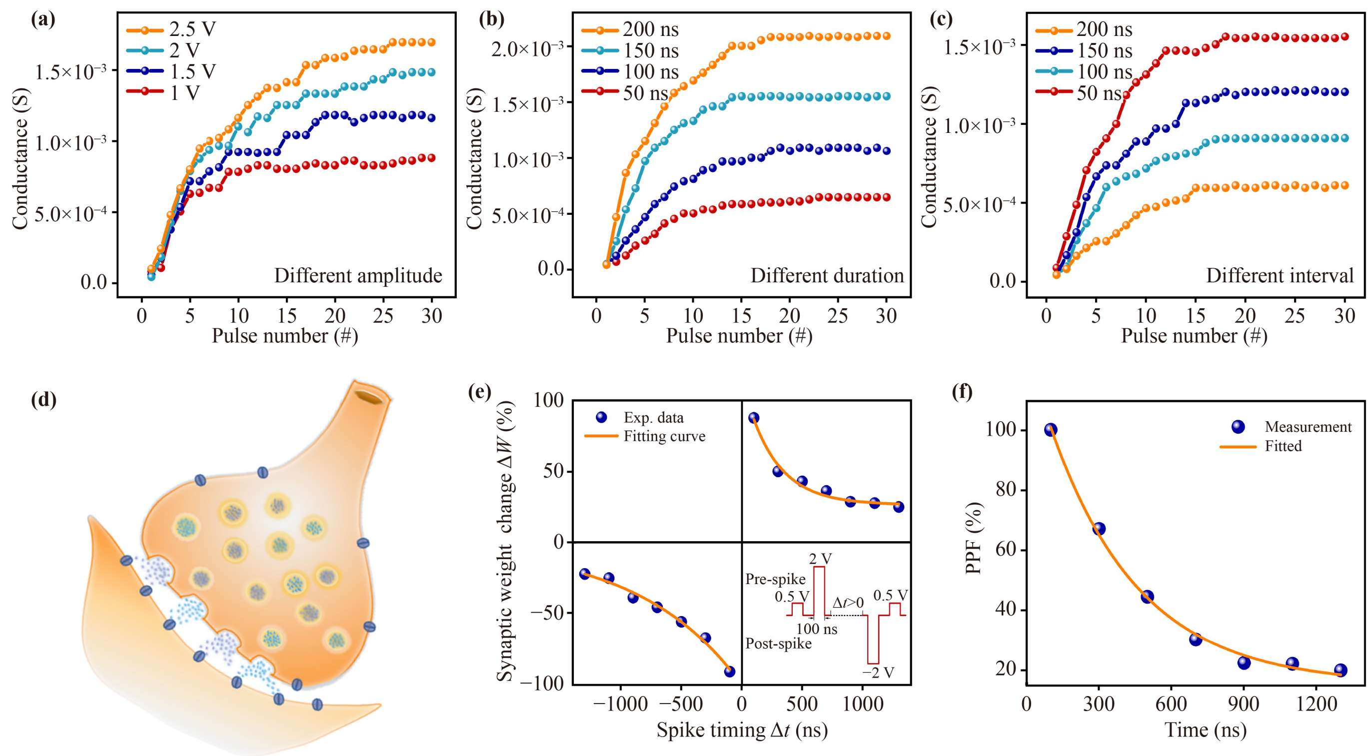

Fig. 5 The device simulates the changes in synaptic weights. **(a–c)** Influence of positive pulses of different amplitudes, durations, and intervals of 30 cycles on conductance modulation. **(d)** Schematic diagram of synaptic structure. **(e)** By changing Δt, realize the STDP function. **(f)** By changing Δt, realize the PPF function.

device conductance changes faster as the pulse duration increases, as shown in Fig. 5(b). Under different pulse interval modulations, the time interval is inversely proportional to the speed of change in the device's conductance, as shown in Fig. 5(c). Figure S6 of the ESM shows the dependence of device conductance on negative pulses. The results show that the conductance of the Ag/STO/Pt device can be adjusted successfully by different pulse parameters of nanosecond level [40, 41], and it is conducive to the fabrication of ultra-fast brain-like neurochips.

In addition, the Hebbian learning rule is a significant conclusion of synaptic plasticity. STDP is one of Hebbian's critical learning rules, which affects the synaptic weight by changing the timing between the pre-spike and post-spike. For the Ag/STO/Pt device, the Ag and the Pt electrodes are analogous to the pre-spike membrane and post-spike membrane, respectively. The changes in the relative conductance (ΔW) of the device were observed by stimulating the two with different time differences (Δt). If pre-spike precedes post-spike ($\Delta t > 0$), the intensity of synaptic connection between two neurons increases, forming the LTP process. On the contrary, if the post-pike precedes the pre-spike ($\Delta t < 0$), the strength of synaptic connection between two neurons decreases, forming the LTD process [42, 43]. Pulse waveform simulating STDP rules is set for testing, and the change of ΔW with Δt can be shown in Fig. 5(e). The LTP and LTD processes are successfully realized, confirming that STDP characteristics of the biological synapse can be simulated on this device. PPF is another vital feature in biological synapses. When two consecutive pulses stimulate a synaptic, the response of the post-pulse is higher than that of the pre-pulse. With the increase of the interval between the two pulses, the response of the post-pulse decrease [44–47]. Figure 5(f) shows that the PPF phenomenon was successfully simulated by applying two pulses of 100 ns duration and 1 V amplitude to the device. These results confirm that the synaptic weight change of the Ag/STO/Pt memristor is controllable, which is the same as the biological synapse. Therefore, the Ag/STO/Pt device provides a pathway for the learning and computation of synaptic signals.

4 Conclusion

In summary, two characteristics of volatile threshold RS and nonvolatile bipolar RS are observed in Ag/STO/Pt device, which depends on the strength of Ag conductive filament in amorphous STO thin-film. When $I_{cc} = 1 \times 10^{-6}$ A, the device exhibits volatile threshold RS and successfully simulates the LIF function of artificial neurons by pulse regulation and bionic circuit design. When $I_{cc} = 1 \times 10^{-3}$ A, the device implements

nonvolatile bipolar RS behavior and simulates the functions of STDP and PPF, which is confirmed to be consistent with the behavior of biological synapses. The device enables the possibility of simulating biological nerves as both artificial synapses and neurons. Therefore, the reconfigurable memristor based on Ag/STO/Pt accelerates the development of the integrated neural chip system.

Conflicts of interest There are no conflicts to declare.

Electronic supplementary materials The online version contains supplementary material available at https://doi.org/10.1007/s11467-023-1308-0 and https://journal.hep.com.cn/fop/EN/10.1007/s11467-023-1308-0.

Acknowledgements This work was financially supported by the National Key R&D Program of China (Grant No. 2018AAA0103300), the National Key R&D Plan "Nano Frontier" Key Special Project (Grant No. 2021YFA1200502), the Cultivation Projects of National Major R&D Project (Grant No. 92164109), the National Natural Science Foundation of China (Grant Nos. 61874158, 62004056, and 62104058), the Special Project of Strategic Leading Science and Technology of Chinese Academy of Sciences (Grant No. XDB44000000-7), Hebei Basic Research Special Key Project (Grant No. F2021201045), the Support Program for the Top Young Talents of Hebei Province (Grant No. 70280011807), the Supporting Plan for 100 Excellent Innovative Talents in Colleges and Universities of Hebei Province (Grant No. SLRC2019018), the Interdisciplinary Research Program of Natural Science of Hebei University (No. DXK202101), Institute of Life Sciences and Green Development (No. 521100311), the Natural Science Foundation of Hebei Province (Nos. F2022201054 and F2021201022), the Outstanding Young Scientific Research and Innovation team of Hebei University (Grant No. 605020521001), Special Support Funds for National High Level Talents (Grant No. 041500120001), High-level Talent Research Startup Project of Hebei University (Grant No. 521000981426), the Science and Technology Project of Hebei Education Department (Grant Nos. QN2020178 and QN2021026), and Baoding Science and Technology Plan Project (Nos. 2172P011 and 2272P014).

References

1. X. Yan, H. He, G. Liu, Z. Zhao, Y. Pei, P. Liu, J. Zhao, Z. Zhou, K. Wang, and H. Yan, A robust memristor based on epitaxial vertically aligned nanostructured $BaTiO_3$–CeO_2 films on silicon, *Adv. Mater.* 34(23), 2110343 (2022)
2. X. Zhang, Y. Zhuo, Q. Luo, Z. Wu, R. Midya, Z. Wang, W. Song, R. Wang, N. K. Upadhyay, Y. Fang, F. Kiani, M. Rao, Y. Yang, Q. Xia, Q. Liu, M. Liu, and J. J. Yang, An artificial spiking afferent nerve based on Mott memristors for neurorobotics, *Nat. Commun.* 11(1), 51 (2020)
3. P. A. Merolla, J. V. Arthur, R. Alvarez-Icaza, A. S. Cassidy, J. Sawada, F. Akopyan, B. L. Jackson, N. Imam, C. Guo, Y. Nakamura, B. Brezzo, I. Vo, S. K. Esser, R. Appuswamy, B. Taba, A. Amir, M. D. Flickner, W. P. Risk, R. Manohar, and D. S. Modha, A million spiking-neuron integrated circuit with a scalable communication network and interface, *Science* 345(6197), 668 (2014)
4. X. Yan, Y. Li, J. Zhao, and Z. Zhou, Bistable capacitance performance-induced ambipolar charge injected based on $Ba_{0.6}Sr_{0.4}TiO_3$ by an Inlaid Zr–Hf–O layer for novel nonvolatile memory application, *IEEE Trans. Electron Dev.* 64(2), 587 (2017)
5. J. M. Nageswaran, N. Dutt, J. L. Krichmar, A. Nicolau, and A. V. Veidenbaum, A configurable simulation environment for the efficient simulation of large-scale spiking neural networks on graphics processors, *Neural Netw.* 22(5–6), 791 (2009)
6. R. Guo, W. Lin, X. Yan, T. Venkatesan, and J. Chen, Ferroic tunnel junctions and their application in neuromorphic networks, *Appl. Phys. Rev.* 7(1), 011304 (2020)
7. H. Ling, D. A. Koutsouras, S. Kazemzadeh, Y. Van De Burgt, F. Yan, and P. Gkoupidenis, Electrolyte-gated transistors for synaptic electronics, neuromorphic computing, and adaptable biointerfacing, *Appl. Phys. Rev.* 7(1), 011307 (2020)
8. Y. Zhang, Z. Wang, J. Zhu, Y. Yang, M. Rao, W. Song, Y. Zhuo, X. Zhang, M. Cui, L. Shen, R. Huang, and J. Joshua Yang, Brain-inspired computing with memristors: Challenges in devices, circuits, and systems, *Appl. Phys. Rev.* 7(1), 011308 (2020)
9. Z. Zhou, F. Yang, S. Wang, L. Wang, X. Wang, C. Wang, Y. Xie, and Q. Liu, Emerging of two-dimensional materials in novel memristor, *Front. Phys.* 17(2), 23204 (2022)
10. H. T. Zhang, T. J. Park, A. Islam, D. S. J. Tran, S. Manna, Q. Wang, S. Mondal, H. Yu, S. Banik, S. Cheng, H. Zhou, S. Gamage, S. Mahapatra, Y. Zhu, Y. Abate, N. Jiang, S. Sankaranarayanan, A. Sengupta, C. Teuscher, and S. Ramanathan, Reconfigurable perovskite nickelate electronics for artificial intelligence, *Science* 375(6580), 533 (2022)
11. H. M. Huang, R. Yang, Z. H. Tan, H. K. He, W. Zhou, J. Xiong, and X. Guo, Quasi-hodgkin–huxley neurons with leaky integrate-and-fire functions physically realized with memristive devices, *Adv. Mater.* 31(3), 1803849 (2019)
12. S. H. Sung, T. J. Kim, H. Shin, T. H. Im, and K. J. Lee, Simultaneous emulation of synaptic and intrinsic plasticity using a memristive synapse, *Nat. Commun.* 13, 2811 (2022)
13. N. Ilyas, J. Wang, C. Li, H. Fu, D. Li, X. Jiang, D. Gu, Y. Jiang, and W. Li, Controllable resistive switching of STO: Ag/SiO_2-based memristor synapse for neuromorphic computing, *J. Mater. Sci. Technol.* 97, 254 (2022)
14. T. Tuma, A. Pantazi, M. Le Gallo, A. Sebastian, and E. Eleftheriou, Stochastic phase-change neurons, *Nat. Nanotechnol.* 11(8), 693 (2016)
15. X. Yan, J. Zhao, S. Liu, Z. Zhou, Q. Liu, J. Chen, and X. Y. Liu, Memristor with Ag-cluster-doped TiO_2 films as artificial synapse for neuroinspired computing, *Adv. Funct. Mater.* 28(1), 1705320 (2018)
16. X. Sun, G. Li, X. Zhang, L. Ding, and W. Zhang, Coexistence of the bipolar and unipolar resistive switching behaviours in $Au/SrTiO_3/Pt$ cells, *J. Phys. D Appl.*

Phys. 44(12), 125404 (2011)

17. J. Ji, F. Ling, S. Zhou, D. Li, C. Luo, L. Wu, and J. Yao, Optically tuned dielectric property of ferroelectric PZT/STO/PT superlattice by THz spectroscopy, *J. Alloys Compd.* 703, 517 (2017)
18. H. Jong Choi, S. Won Park, G. Deok Han, J. Na, G. T. Kim, and J. Hyung Shim, Resistive switching characteristics of polycrystalline $SrTiO_3$ films, *Appl. Phys. Lett.* 104(24), 242105 (2014)
19. X. Yan, J. Yin, Z. Liu, and X. Xia, Studies on the reset power needed for the unipolar resistive switching in amorphous $SrTiO_{3-\delta}$ films induced by electrical pulse, *Phys. Lett. A* 375(41), 3599 (2011)
20. P. Hou, Z. Gao, and K. Ni, Multilevel data storage memory based on polycrystalline $SrTiO_3$ ultrathin film, *RSC Advances* 7(78), 49753 (2017)
21. H. Hu, Y. Li, Y. Yang, W. Lv, H. Yu, W. Lu, Y. Dong, and Z. Wen, Enhanced resistance switching in ultrathin Ag/$SrTiO_3$/(La, Sr)MnO_3 memristors and their long-term plasticity for neuromorphic computing, *Appl. Phys. Lett.* 119(2), 023502 (2021)
22. J. Xiong, R. Yang, J. Shaibo, H. M. Huang, H. K. He, W. Zhou, and X. Guo, Bienenstock, Cooper, and Munro learning rules realized in second-order memristors with tunable forgetting rate, *Adv. Funct. Mater.* 29(9), 1807316 (2019)
23. M. A. Rahman, S. Walia, S. Naznee, M. Taha, S. Nirantar, F. Rahman, M. Bhaskaran, and S. Sriram, Artificial somatosensors: Feedback receptors for electronic skins, *Adv. Intell. Syst.* 2(11), 2000094 (2020)
24. H. Tang, X. G. Tang, Y. P. Jiang, Q. X. Liu, W. H. Li, and L. Luo, Bipolar resistive switching characteristics of amorphous $SrTiO_3$ thin films prepared by the sol–gel process, *J Asian Ceram Soc.* 7(3), 298 (2019)
25. K. Wang, Q. Hu, B. Gao, Q. Lin, F. W. Zhuge, D. Y. Zhang, L. Wang, Y. H. He, R. H. Scheicher, H. Tong, and X. S. Miao, Threshold switching memristor-based stochastic neurons for probabilistic computing, *Mater. Horiz.* 8(2), 619 (2021)
26. K. Wang, L. Li, R. Zhao, J. Zhao, Z. Zhou, J. Wang, H. Wang, B. Tang, C. Lu, J. Lou, J. Chen, and X. Yan, A pure 2H-MoS_2 nanosheet-based memristor with low power consumption and linear multilevel storage for artificial synapse emulator, *Adv. Electron. Mater.* 6(3), 1901342 (2020)
27. G. Wang, X. Yan, J. Chen, and D. Ren, Memristors based on the hybrid structure of oxide and boron nitride nanosheets combining memristive and neuromorphic functionalities, *Phys. Status Solidi Rapid Res. Lett.* 14(1), 1900539 (2020)
28. F. Wu, S. Si, P. Cao, W. Wei, X. Zhao, T. Shi, X. Zhang, J. Ma, R. Cao, L. Liao, T. Y. Tseng, and Q. Liu, Interface engineering via MoS_2 insertion layer for improving resistive switching of conductive-bridging random access memory, *Adv. Electron. Mater.* 5(4), 1800747 (2019)
29. L. A. Liu, J. Zhao, G. Cao, S. Zheng, and X. Yan, A memristor-based silicon carbide for artificial nociceptor and neuromorphic computing, *Adv. Electron. Mater.* 6, 2100373 (2021)
30. X. Mou, J. Tang, Y. Lyu, Q. Zhang, S. Yang, F. Xu, W. Liu, M. Xu, Y. Zhou, W. Sun, Y. Zhong, B. Gao, P. Yu, H. Qian, and H. Wu, Analog memristive synapse based on topotactic phase transition for high-performance neuromorphic computing and neural network pruning, *Sci. Adv.* 7(29), eabh0648 (2021)
31. Y. Zhang, W. He, Y. Wu, K. Huang, Y. Shen, J. Su, Y. Wang, Z. Zhang, X. Ji, G. Li, H. Zhang, S. Song, H. Li, L. Sun, R. Zhao, and L. Shi, Highly compact artificial memristive neuron with low energy consumption, *Small* 14(51), 1802188 (2018)
32. Y. Zhang, Z. Fang, and X. Yan, HfO_2-based memristor-CMOS hybrid implementation of artificial neuron model, *Appl. Phys. Lett.* 120(21), 213502 (2022)
33. L. Yan, Y. Pei, J. Wang, H. He, Y. Zhao, X. Li, Y. Wei, and X. Yan, High-speed Si films based threshold switching device and its artificial neuron application, *Appl. Phys. Lett.* 119(15), 153507 (2021)
34. Y. Wang, X. Chen, D. Shen, M. Zhang, X. Chen, X. Chen, W. Shao, H. Gu, J. Xu, E. Hu, L. Wang, R. Xu, and Y. Tong, Artificial neurons based on Ag/V_2C/W threshold switching memristors, *Nanomaterials (Basel)* 11(11), 2860 (2021)
35. P. Dayan and L. F. Abbott, Theoretical Neuroscience: Computational and Mathematical Modeling of Neural Systems, MIT Press, 2005
36. R. Yang, H. M. Huang, Q. H. Hong, X. B. Yin, Z. H. Tan, T. Shi, Y. X. Zhou, X. S. Miao, X. P. Wang, S. B. Mi, C. L. Jia, and X. Guo, Synaptic suppression triplet-STDP learning rule realized in second-order memristors, *Adv. Funct. Mater.* 28(5), 1704455 (2018)
37. Y. He, S. Nie, R. Liu, S. Jiang, Y. Shi, and Q. Wan, Spatiotemporal information processing emulated by multiterminal neuro-transistor networks, *Adv. Mater.* 31(21), 1900903 (2019)
38. X. Zhang, W. Wang, Q. Liu, X. Zhao, J. Wei, R. Cao, Z. Yao, X. Zhu, F. Zhang, and H. Lv, An artificial neuron based on a threshold switching memristor, *IEEE Electr. Device L.* 39(2), 308 (2017)
39. G. Cao, X. Yan, J. Wang, Z. Zhou, J. Lou, and K. Wang, Realization of fast switching speed and electronic synapse in Ta/TaO_x/AlN/Pt bipolar resistive memory, *AIP Adv.* 10(5), 055312 (2020)
40. X. Yan, K. Wang, J. Zhao, Z. Zhou, H. Wang, J. Wang, L. Zhang, X. Li, Z. Xiao, Q. Zhao, Y. Pei, G. Wang, C. Qin, H. Li, J. Lou, Q. Liu, and P. Zhou, A new memristor with 2D $Ti_3C_2T_x$ MXene flakes as an artificial bio-synapse, *Small* 15(25), 1900107 (2019)
41. Z. Zhao, A. Abdelsamie, R. Guo, S. Shi, J. Zhao, W. Lin, K. Sun, J. Wang, J. Wang, X. Yan, and J. Chen, Flexible artificial synapse based on single-crystalline $BiFeO_3$ thin film, *Nano Res.* 15(3), 2682 (2022)
42. T. Shi, R. Wang, Z. Wu, Y. Sun, J. An, and Q. Liu, A review of resistive switching devices: Performance improvement, characterization, and applications, *Small Struct.* 2(4), 2000109 (2021)
43. Y. Pei, Z. Zhou, A. P. Chen, J. Chen, and X. Yan, A carbon-based memristor design for associative learning activities and neuromorphic computing, *Nanoscale* 12(25), 13531 (2020)
44. Y. F. Wang, Y. C. Lin, I. T. Wang, T. P. Lin, and T. H. Hou, Characterization and modeling of nonfilamentary

$Ta/TaO_x/TiO_2/Ti$ analog synaptic device, *Sci. Rep.* 5(1), 10150 (2015)

45. Z. Zhao and X. Yan, Ferroelectric memristor based on $Hf_{0.5}Zr_{0.5}O_2$ thin film combining memristive and neuromorphic functionalities, *Phys. Status Solidi Rapid Res. Lett.* 14(9), 2000224 (2020)
46. Z. Zhu, Y. Pei, C. Gao, H. Wang, and X. Yan, A Cu/HZO/GeS/Pt memristor for neuroinspired computing, *Phys. Status Solidi Rapid Res. Lett.* 15(10), 2100072 (2021)
47. S. Ke, L. Jiang, Y. Zhao, Y. Xiao, B. Jiang, G. Cheng, F. Wu, G. Cao, Z. Peng, M. Zhu, and C. Ye, Brain-like synaptic memristor based on lithium-doped silicate for neuromorphic computing, *Front. Phys.* 17(5), 53508 (2022)